

Multiphase, Multiscale Chemomechanics at Extreme Low Temperatures: Battery Electrodes for Operation in a Wide Temperature Range

Jizhou Li, Shaofeng Li, Yuxin Zhang, Yang Yang, Silvia Russi, Guannan Qian, Linqin Mu, Sang-Jun Lee, Zhijie Yang, Jun-Sik Lee, Piero Pianetta, Jieshan Qiu, Daniel Ratner, Peter Cloetens,* Kejie Zhao,* Feng Lin,* and Yijin Liu*

Understanding the behavior of lithium-ion batteries (LIBs) under extreme conditions, for example, low temperature, is key to broad adoption of LIBs in various application scenarios. LIBs, poor performance at low temperatures is often attributed to the inferior lithium-ion transport in the electrolyte, which has motivated new electrolyte development as well as the battery preheating approach that is popular in electric vehicles. A significant irrevocable capacity loss, however, is not resolved by these measures nor well understood.

Herein, multiphase, multiscale chemomechanical behaviors in composite $\text{LiNi}_x\text{Mn}_y\text{Co}_z\text{O}_2$ (NMC, $x + y + z = 1$) cathodes at extremely low temperatures are systematically elucidated. The low-temperature storage of LIBs can result in irreversible structural damage in active electrodes, which can negatively impact the subsequent battery cycling performance at ambient temperature. Beside developing electrolytes that have stable performance, designing batteries for use in a wide temperature range also calls for the development of electrode components that are structurally and morphologically robust when the cell is switched between different temperatures.

source in applications ranging from consumer electronics to electric vehicles. There is an increasing desire for stable storage and utilization of electrical energy under extreme conditions such as cold-climate, aerospace exploration, and subsea operations. These applications feature highly diverse and varying working environments with overcharge/discharge, high pressure, external forces, and often most critical, high/low temperature.^[1–4] For example, LIBs lose most of their capacity, power, and cycle life when operated below ambient temperature. It has been reported that, at -40°C , conventional LIBs only retained $\approx 12\%$ of their room-temperature capacity.^[5] This has necessitated a thermal management component as an accessory to the battery system,^[6] which not only complicates the storage and operation but also exerts some negative effects on LIBs,^[3]

for example, decreasing the cycle life due to cell temperature inhomogeneity. Therefore, it is crucial to gain more insights into the mechanisms causing the LIB performance degradation upon exposure to low-temperature conditions, which

1. Introduction

Lithium-ion battery (LIB), a tremendously successful technology for energy storage, has become the dominant power

J. Li, S. Li, S. Russi, G. Qian, S.-J. Lee, J.-S. Lee, P. Pianetta, Y. Liu
Stanford Synchrotron Radiation Lightsource
SLAC National Accelerator Laboratory
Menlo Park, CA 94025, USA
E-mail: liuyijin@slac.stanford.edu

S. Li, J. Qiu
State Key Lab of Fine Chemicals
School of Chemical Engineering
Liaoning Key Lab for Energy Materials and Chemical Engineering
Dalian University of Technology
Dalian 116024, China

Y. Zhang, L. Mu, Z. Yang, F. Lin
Department of Chemistry
Virginia Tech
Blacksburg, VA 24061, USA
E-mail: fenglin@vt.edu

 The ORCID identification number(s) for the author(s) of this article can be found under <https://doi.org/10.1002/aenm.202102122>.

Y. Yang, P. Cloetens
European Synchrotron Radiation Facility
Grenoble 38000, France
E-mail: Cloetens@esrf.fr

Y. Yang
National Synchrotron Light Source II
Brookhaven National Laboratory
Upton, NY 11973, USA

D. Ratner
Machine Learning Initiative
SLAC National Accelerator Laboratory
Menlo Park, CA 94025, USA

K. Zhao
School of Mechanical Engineering
Purdue University
West Lafayette, IN 47906, USA
E-mail: kjzhao@purdue.edu

DOI: 10.1002/aenm.202102122

could aid engineering of active materials, electrode structure, and charge/discharge protocols.^[2]

Previous studies^[1–3] have utilized several enlightened approaches to analyze the decreased capacity of LIBs and have identified various factors that could deteriorate the LIB performance at low temperatures. The sluggish lithium-ion diffusion in the electrolyte is generally regarded as the main reason for the unsatisfactory LIB performance under low-temperature conditions. It can also cause interfacial problems, for example, lithium dendrite growth on the anode surface.^[7] This has motivated efforts in designing new electrolytes and electrolyte additives that could improve lithium-ion conductivity in the electrolyte at low temperatures. Nevertheless, the rate capability of LIBs still drops significantly when the temperature decreases to below ambient, especially during the charging process.^[8]

Beyond the temperature-dependent lithium-ion conductivity in the electrolyte, more complications have been reported. For example, it has been demonstrated that the low-temperature performance of LIBs can be improved by using liquefied gas or ethyl acetate as electrolyte solvent.^[9,10] Xu et al.^[11] demonstrated a LIB that can deliver $\approx 60\%$ of its room-temperature capacity at $-80\text{ }^\circ\text{C}$ by increasing the lithium diffusion rate across the liquid-solid interfaces. Dong et al.^[12] reported that the low-temperature behaviors of LIBs are limited by the slow Li^+ desolvation even when the ionic conductivity is sufficient in the electrolyte and no solid electrolyte interphases (SEIs) are formed on the electrodes. These literatures collectively suggest that, in addition to the kinetic factors involving the lithium-ion diffusion through electrolyte and SEI, there are other effects that could significantly impact the performance of LIBs under low-temperature conditions. More importantly, these effects can be irreversible as a significant degree of irrevocable performance deterioration is often seen as inevitable upon exposure to low-temperature conditions. Such irreversibility still holds even if the cell is cycled after being brought back to the ambient temperature. Therefore, an in-depth, systematic investigation is pivotal to truly unveil the LIBs behavior associated with the low-temperature environment.

In this work, we investigate the structural deformation and mechanical damage of LIB composite $\text{LiNi}_x\text{Mn}_y\text{Co}_z\text{O}_2$ (NMC, $x + y + z = 1$) cathode upon exposure to low-temperature (low-T) conditions. By utilizing a suite of advanced characterization techniques including synchrotron-based x-ray powder diffraction (XRD), X-ray absorption near edge structure (XANES), extended X-ray absorption fine structure (EXAFS), full-field transmission X-ray microscopy (TXM), and X-ray phase contrast nano-holo-tomography, we systematically elucidate the multiphase multiscale chemomechanics in the battery cathode at low temperatures. We observe that, upon exposure to low temperature and then recover to room temperature, the reversible and anisotropic lattice deformation could lead to irreversible cracking of active cathode particles. At the electrode scale, the morphological deformations of different cathode components mismatch at low temperatures, causing structural disintegration that could irreversibly provoke the development of local impedance and particle deactivation. Our results suggest that, in order to design batteries for use in a wide temperature range, it is critical to develop electrode components that are structurally and morphologically robust when the cell is switched between different temperatures.

2. Results

2.1. Electrochemical Characterization after Exposure to Low-Temperature Environments

We first investigate how the low-temperature storage may influence battery performance at ambient temperature. **Figure 1** shows the result of our electrochemical measurements using a Ni-rich layered transition metal oxides cathode and the corresponding absolute specific capacity decay is shown in Figure S1, Supporting Information. We first cycle the cells at room temperature (RT) for 20 cycles and then pause the cycling procedure at the discharged state, followed by a controlled temperature-controlled storage (T-storage) process. More specifically, we store the cells at different temperatures (RT, $0\text{ }^\circ\text{C}$, $-20\text{ }^\circ\text{C}$, and $-80\text{ }^\circ\text{C}$) for 48 h and bring them to RT and store for another 48 h. Subsequently, we resume the electrochemical cycling to monitor the impact of low-temperature storage on battery performance. Note that the cells that have not been exposed to the low-temperature conditions serve as the baseline. We perform these experiments at two different charging rates (1 and 5 C). In general, the electrochemical performance of cells gets compromised after the low-temperature storage regardless of the charging rates. While the low-temperature storage has only minor impact on the battery performance at 1 C, we observe that it has a more significant impact on the high-rate cycling performance (5 C). The capacity fading is accelerated after the low-temperature storage in both cases/charging rates. Since all electrochemical cycling is performed at room temperature, we conjecture that the accelerated capacity fading after the storage is ascribed to the irreversible degradation of electrodes during the low-temperature storage. This observation motivates a systematic study on the structural deformation and mechanical damage of cathode during low-temperature storage.

To delineate the degradations of Li-metal anode, we assemble Li symmetric cells and adopt the same storage experiments at low temperatures to investigate the variation of their electrochemical performance and overall impedance. From Figure S2a–c, Supporting Information, we can observe that low-temperature storage does not compromise the Li metal performance even at a very high current density. Moreover, Figure S2d–f, Supporting Information, tells us that the Li symmetric cells stored at different temperatures exhibit similar impedance, which is in line with our charging-discharging results and confirms the negligible influence induced by the Li-metal anode at low temperatures.

Moreover, we performed the cyclic voltammetry (CV) measurements to the cells stored at 25 and $-80\text{ }^\circ\text{C}$ due to the significant difference of electrochemical degradation behavior between them. As shown in Figure S3, Supporting Information, we find that after storing at $25\text{ }^\circ\text{C}$, the CV profiles are almost identical upon following 20 cycles. However, for the cells stored at $-80\text{ }^\circ\text{C}$, we can still observe obvious current decay, especially at high-voltage upon following cycles, indicating that the electrochemical stability is compromised after low-temperature storage.

To show the evolution of cell impedance after low-temperature storage, we conduct the electrical impedance spectroscopy measurements to the cells stored at different temperatures

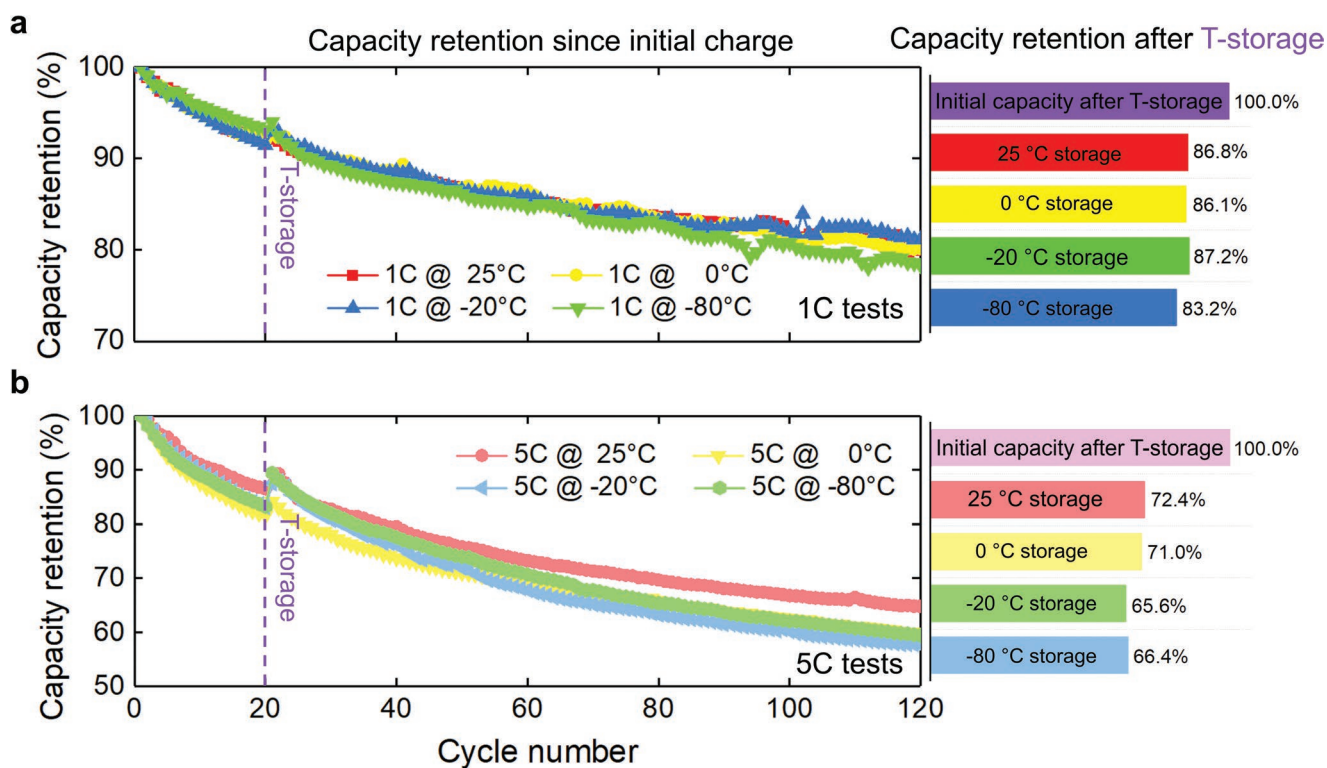


Figure 1. Electrochemical performance. The capacity retention of batteries before and after the exposure to low-temperature environment under two different current rates, a) 1 C and b) 5 C, for comparison. The initial discharge capacity is set as the baseline to show the overall decay upon electrochemical cycling in the figure to the left, while the discharge capacity of the first cycle after T-storage is regarded as the baseline in the figure to the right to show the capacity retention after 100 cycles at different C rates.

(0, -20, and -80 °C). Our results in Figure S4, Supporting Information, suggest that after low-temperature storage, although the impedance coming from surface-interphase does not show significant change, the charge transfer resistance increases dramatically, especially at -80 °C. The enlarged impedance can retard the charge transfer and compromise the electrochemical performance in the following cycles, partially explaining the origin of more severe decay when cells are stored at low temperatures.

2.2. Evolutions of NMC Cathode's Crystal and Electronic Structures at Low Temperatures

To understand the low-temperature induced lattice deformation and strain at the atomic scale, here we employ a few experimental methods that are sensitive to the local lattice and electronic structures. We conducted X-ray absorption spectroscopic measurements over the Ni K-edge for the charged NMC electrode. As shown in Figure 2a, the X-ray absorption spectra were measured under three different conditions, for example, room temperature (RT, 25 °C), -173 °C, and recovered to RT (denoted as Rec). It appears that, in the XANES region, there are no noticeable differences except for a very small increment of the pre-edge peak at -173 °C. The pre-edge peak arises from 1s to 3d transition, which is sensitive to the symmetry of the surrounding atoms. The low-temperature-induced increment of the pre-edge peak intensity indicates a distorted octahedral

structure at the low temperature. To further elucidate the local coordination environment of Ni atoms, the Fourier transform (FT) of the extended XAFS (FT-EXAFS) spectra at the Ni K-edge are shown in Figure 2b. The FT curves of the electrode under different conditions reveal that the intensity of the peak at 2.48 Å significantly increases at -173 °C, indicating an increased Ni-M (M represents Ni, Co, Mn) coordination number for the Ni sites. Note that metal cations do not form direct chemical bonds and the Ni-M coordination number denotes the average number of transition metal cations surrounding the Ni center at a distance of 2.48 Å. The similar phenomenon is also observed in the wavelet transform analyses for the Ni K-edge EXAFS (WT-EXAFS), which is confirmed by the increased intensity maximum at $\approx 8 \text{ \AA}^{-1}$ (assigned to Ni-M interatomic distance) at -173 °C (Figure 2c). In addition, the slight positive shift of Ni-O peak in Figure 2b further implies an increase in the Ni-O atomic distance at -173 °C.

To accurately reconstruct the coordination configuration centered around the Ni atoms at different temperatures, we turn to quantitative EXAFS fitting for extracting the structure parameters. As shown in Figure 2d,e and the EXAFS fitting results (Figure S5 and Table S1, Supporting Information), the Ni-O atomic distance ($R(\text{Ni-O})$) is increased from 1.89 to 1.94 Å at -173 °C, and then decreased to 1.90 Å after being recovered to RT. On the contrary, the Ni-M atomic distance ($R(\text{Ni-M})$) is decreased from 2.85 to 2.81 Å at -173 °C, and then increased to 2.84 Å after being recovered to RT. This indicates a compressive strain of 1.4% at -173 °C. Besides, the Ni-M coordination

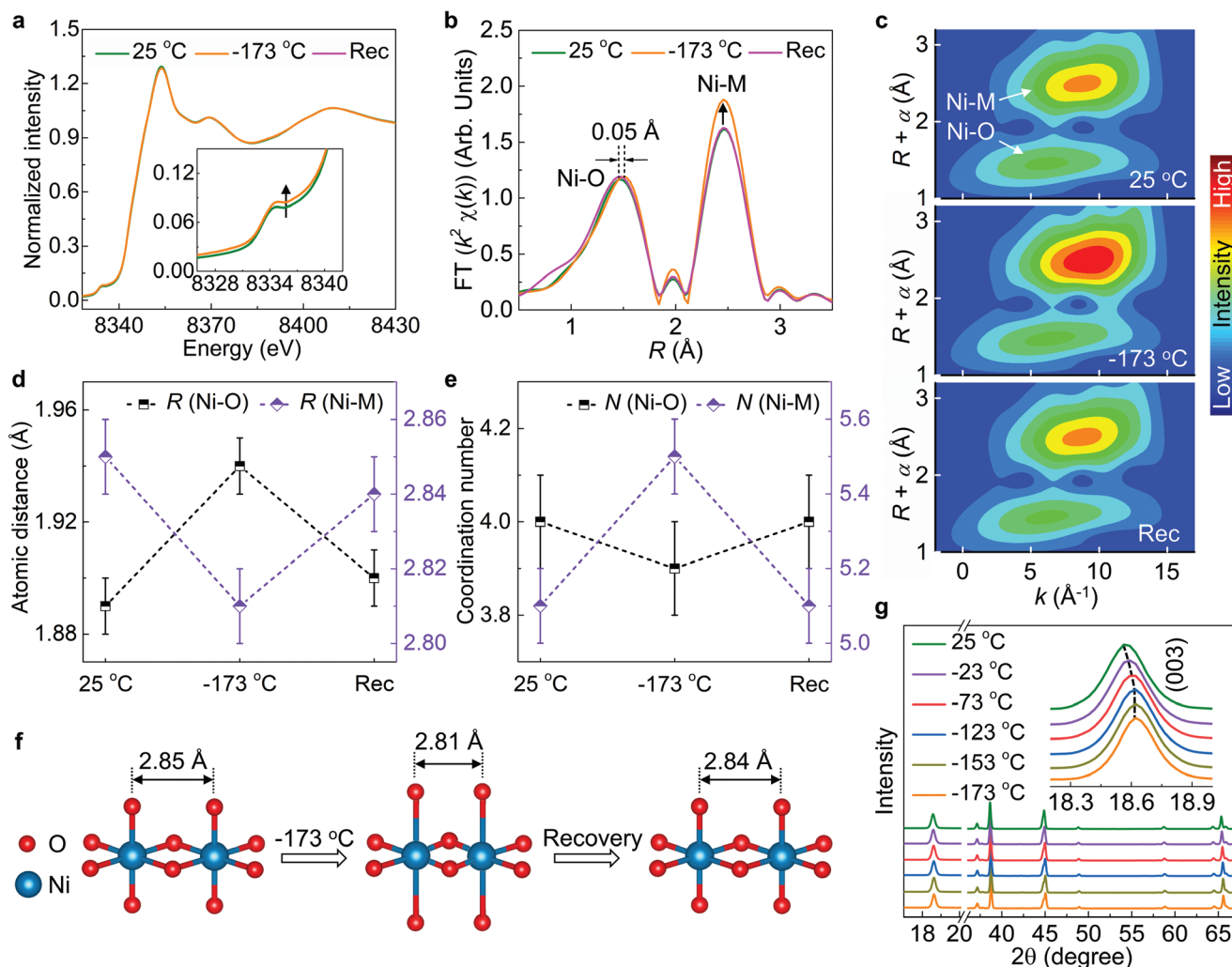


Figure 2. Structure characterization of the charged NMC electrode under different conditions. The temperature dependent a) XANES spectra, b) FT-EXAFS spectra, and c) WT-EXAFS maps recorded at Ni K-edge. d) Atomic distance and e) coordination number of the Ni–O and Ni–M under different temperatures retrieved via EXAFS fitting, showing the reversible low-temperature-induced lattice deformation. f) Schematic showing the structure evolution of the octahedral structure upon exposing to low temperature and then recovering to RT. g) In situ XRD patterns on the charged NMC electrode as the temperature is lowered from 25 to -173 °C.

number ($N(\text{Ni-M})$) is increased from 5.1 to 5.5 at -173 °C, and then back to 5.1 after being recovered to RT. Compared with $N(\text{Ni-M})$, the Ni–O coordination number ($N(\text{Ni-O})$) is decreased slightly from 4.0 to 3.9 at -173 °C, and then back to 4.0 after being recovered to RT. The increased $N(\text{Ni-M})$ and reduced $N(\text{Ni-O})$ can possibly be ascribed to the reduced $R(\text{Ni-M})$ and increased $R(\text{Ni-O})$ at -173 °C, respectively. As shown in the temperature-dependent XRD patterns (from 25 °C to -173 °C, Figure 2g), the positive shift of (003) peak further indicates the reduced lattice distance, echoing the compressive strain as suggested by the EXAFS results. It is worth noting that the (003) peak shift upon reducing the temperature is relatively more significant at the beginning and saturates around -73 °C. Based on these results, the low-temperature-induced atomic structural evolution of the charged NMC electrode was illustrated schematically in Figure 2f. At -173 °C, $R(\text{Ni-M})$ is decreased accompanied by the increased $R(\text{Ni-O})$, resulting in the compressive strain and distorted octahedral coordination. After recovering to RT, the

distorted lattice configuration is largely recovered. Although the low-temperature-induced lattice deformation is reversible from the atomistic perspective, the compressive strain could lead to the escalation of mechanical stress that has consequences on the morphological integrity at a larger scale. We look into this effect in the next sections. Essentially, we identified a “saturation point” at -73 °C through the low-T XRD, and compared the spectroscopy (XANES and EXAFS) and imaging (TXM and nano-holo-tomography) data above and below this saturation point, which helps us to understand the low-T induced electrode degradation. More clarification on the experimental design is included in the Supporting Information.

2.3. Mesoscale Particle Cracking at Low Temperatures

In this section, we demonstrate that exposing the battery cathode particle to extreme low-temperature conditions can

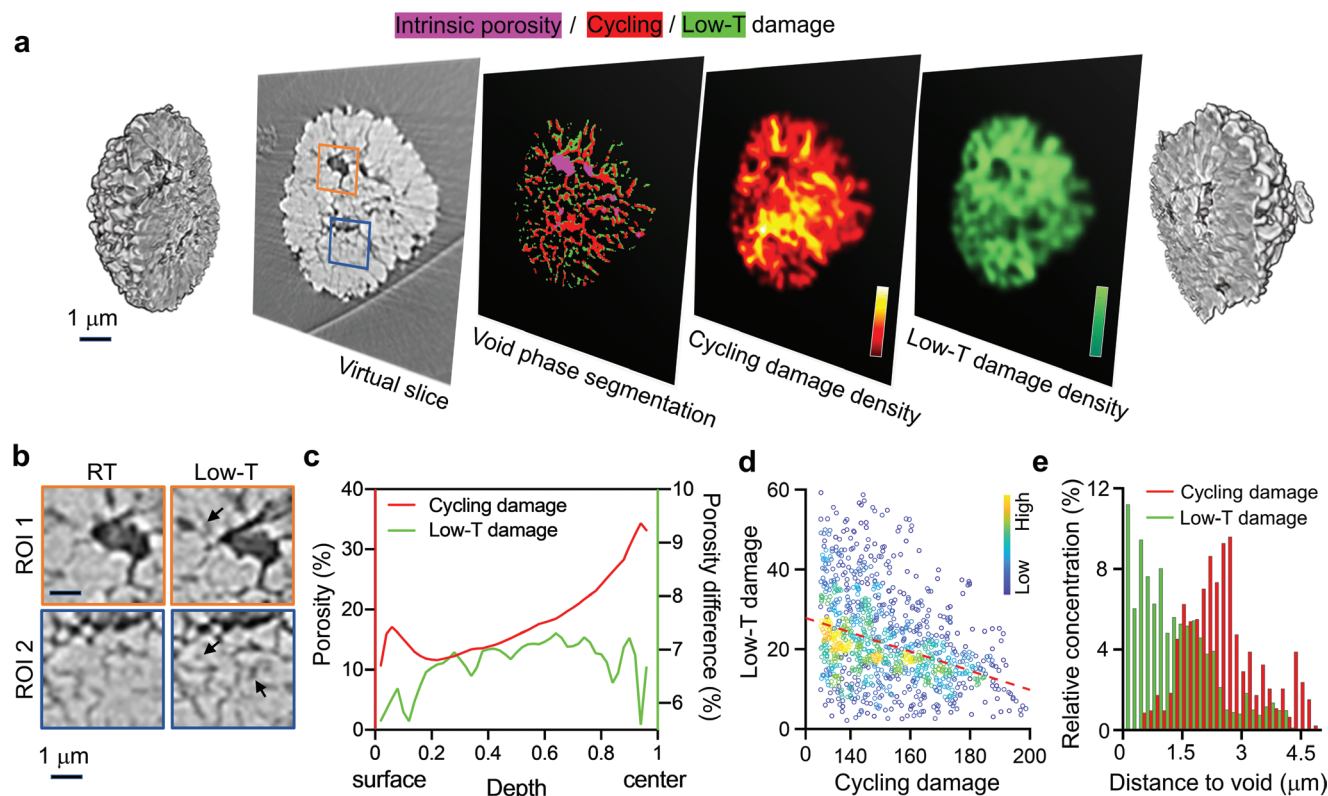


Figure 3. TXM characterization of single NMC particle damages. a) A 3D rendering of single NMC particle with its central slice shown in the middle. The particle's structural damages of different origins are segmented and then used for calculating the local damage density. b) Two selected regions of interest, as indicated in (a), are compared before and after the low-temperature exposure. c) Depth-dependent profiles of the damages caused by electrochemical cycling and by exposure to $-40\text{ }^{\circ}\text{C}$. d) The spatial association of the cycling-induced cracks and the low-temperature-induced damages, showing a mild negative correlation. e) The relative frequency histogram of cycling-induced damage and low-temperature-induced damage as a function of the distance from the nearest pore phase, which suggests a closer association of the low-temperature-induced damage with the intrinsic porosity.

induce irreversible damages. A broadly observed mechanism for releasing the mechanical stress is the particle cracking.^[13] Here, we employ the full-field TXM to conduct in situ nanotomographic imaging of a single NMC cathode particle as the temperature is lowered from RT to $-40\text{ }^{\circ}\text{C}$. More details about this well-established method for mesoscale battery research can be found in the literature.^[14] As visualized in **Figure 3a** and in Movie S1, Supporting Information, in addition to the cycling-induced cracks that exist prior to the low-temperature exposure, additional damages are developed as the temperature is decreased to $-40\text{ }^{\circ}\text{C}$.

A closer look at the spatial arrangement of the cracking patterns over this particle reveals interesting behaviors. We segment the void space within the imaged particle into three different components (see Experimental Section) of including intrinsic porosity (purple), cycling-induced cracks (red), and low-temperature-induced cracks (green). It is useful to note that the pristine particles in our electrode could exhibit some internal porosity but are structurally intact^[15] because the calendaring process was not applied in our laboratory electrode casting procedure. The relative concentration maps of the cracks with different origins are presented in Figure 3a, and two typical ROIs before and after the low-temperature exposure are shown in Figure 3b. More examples can be found in Figure S6, Supporting Information. We first investigate

the degree of the depth-dependence for the cracks with different origins (Figure 3c). While the cycling-induced damage is more severe over the core region of the particle, in good agreement with a number of reported experimental observations,^[16,17] the low-temperature-induced cracks exhibit a rather flat depth-dependence profile. Although the high-resolution images offer a great amount of structural details, it could be overwhelming to the visual assessment. Therefore, we carry out correlation analysis based on the two crack density maps, revealing an interesting spatial anticorrelation as demonstrated by the negative trend in Figure 3d, in which the x-axis and y-axis represent the degrees of cycling and low-T damage densities, respectively. The exposure of the NMC particle to the low-temperature condition predominantly damages the sub-particle regions that are more intact after the electrochemical cycling. To understand this observation, we evaluate the spatial association of the intrinsic porosity with the cracks of different origins. The relative concentration distributions of the cycling damage and low-T damage as a function of the distance to their nearest pore phase are respectively plotted in Figure 3e, showing a higher degree of association between the low-temperature-induced cracks and the particle's intrinsic porosity. It is interesting to note that the intrinsic porosity in a secondary NMC particle is often regarded as a favorable feature from the mechanical perspective, because it could effectively mitigate the

stress accumulation in repeated electrochemical cycling.^[18] It, however, does not play the same role when it comes to the particle's response to the low-temperature environment. With this dilemma in mind, the single-crystalline NMC particle may be a candidate that is robust to both the electrochemical cycling and the extremely low temperature.^[18]

As control experiments, we conducted more TXM imaging under different low-T conditions (0, -20, and -80 °C) to supplement the above presented TXM data at -40 °C. As shown in Figure S7, Supporting Information, the effect on the particle damages induced at low temperature is rather complicated. There is no obvious low-temperature-induced damage observed for 0 °C. Similar to -40, -20, and -80 °C indeed bring additional irreversible damage. This calls for in-depth investigations of low-temperature effects to reinforce the structural integrity. We also conducted a long-time temperature hold at -20 °C in the TXM experiment because this is the most relevant to real-world battery operation in cold climate. The results, shown in Figure S8, Supporting Information, suggest that, the low-temperature-induced damage is quite instantaneous and is less sensitive to the exposure time.

2.4. Composite Cathode Deformation under Low Temperature

On top of the above-discussed behaviors of the active NMC cathode on the atomic and the single-particle scales, at the electrode level, the system is further complicated by the co-existence of multiple phases including the carbon/binder domains (CBD), the pore structure, and the NMC particles. It is a consensus that this multiphase interaction has a significant role to play in affecting battery performance. We explore the electrode-level microstructures utilizing nano-resolution X-ray phase-contrast nano-holo-tomography,^[19] which offers excellent sensitivity to both the dense NMC particles and the porous matrix of low-Z CBD^[20,21] (see visualization of the reconstructed 3D volume and a 2D virtual slice in **Figure 4a,b,c,d** and also **Figure S9**, Supporting Information). The gray values in the reconstructed phase-contrast images are proportional to the real part of the complex refractive index, which is determined by the local electron density of the materials.^[22] The excellent contrast in the quantitatively reconstructed images allows us to distinguish the three different cathode components (NMC, CBD, and pore network) with a good fidelity (see **Figure 4b,c**). We repeat this measurement over the exact same sample region under room temperature and at -133 °C to avoid any ambiguity in evaluating the low-temperature effect. For statistical significance in this analysis, we identified, in total, 558 NMC particles (see **Figure 4b**) in the imaged 3D volume using a machine-learning approach that was developed by our group.^[21] With the temperature-dependent nano-holo-tomographic data as input, we evaluate the deformation of different electrode components separately. As shown in **Figure 4f**, low-temperature-induced deformations of the NMC and CBD appear to be rather incoherent. We further quantify the degrees of particle detachment from the CBD for all the NMC particles before and after the low-temperature exposure (see comparison in **Figure 4d**). The differential value indicates the low-temperature effect and is used to color-code the image shown in **Figure 4e**. A rather

heterogeneous low-temperature effect can be observed as indicated by the kaleidoscopic map in **Figure 4e**, with majority of the particles experiencing an increased detachment from the CBD matrix upon exposure to low-temperature. Further statistical comparison is shown in the inset in **Figure 4e**, which clearly supports our assessment of **Figure 4e**.

For better understanding the low-temperature-induced NMC detachment from CBD, we look into the incoherence in the deformations of NMC, CBD, and the pore phase using a standard deformation estimation algorithm in computer vision.^[23] The 3D visualization of the deformation is shown in **Figure S10**, Supporting Information. The amplitude and orientation of each displacement vector are calculated voxel by voxel and then assigned to different cathode components for further statistical analysis (**Figure 4g-i**). As shown in **Figure 4h**, compared with that of CBD and pore space, the amplitude of the deformation vector for NMC particles is rather insignificant. This finding agrees with our previous observation in the single-particle experiment (as shown in **Figure 3**) that exposure to low-temperature does not lead to very significant volume expansion/contraction for the particle as a whole. On the other hand, the NMC particles are subjected to a more noticeable rotation with the most significant direction being around an in-plane axis (corresponding to the angle γ illustrated in **Figure 4i**). This suggests that, as the temperature is decreased, the porous CBD matrix undergoes a more significant absolute deformation, which causes NMC particle to rotate with respect to a preferred in-plane axis (see the orientational distribution of the deformation vectors in **Figure 4g** and an illustration example in **Figure S11**, Supporting Information) and, subsequently, leads to the NMC-CBD detachment.

3. Conclusion

Understanding the batteries' behavior under extreme conditions constitutes a research frontier that is of tremendous scientific and industrial potential. The multiscale and multiphase complexities in a LIB fundamentally determine that a thorough investigation is indispensable to formulating a strategy of improving the battery robustness against extreme conditions. For low-temperature applications, immense efforts have been devoted to improving lithium-ion transport in the electrolyte and through the SEI. This remains one of the research frontiers. A significant irreversible LIB performance degradation upon exposure to low-temperature conditions, however, is not understood and rarely tackled. Our control experiments using Li symmetric cells show negligible degradation upon exposure to low temperature, which justifies our focus on the cathode's low-temperature behavior. We focused on this topic and carried out a systematic investigation of the battery cathode in the low-temperature environment. We combined a suite of advanced experimental tools to investigate the structural deformation and mechanical damage across a broad range of length scales. We report that, at the atomic scale, the compressive strain and the lattice deformation appear to be reversible upon exposing to low-temperature and then recovering to RT. Under extremely-low temperature, however, the stress could escalate to an extent that will lead to active particle cracking. At the

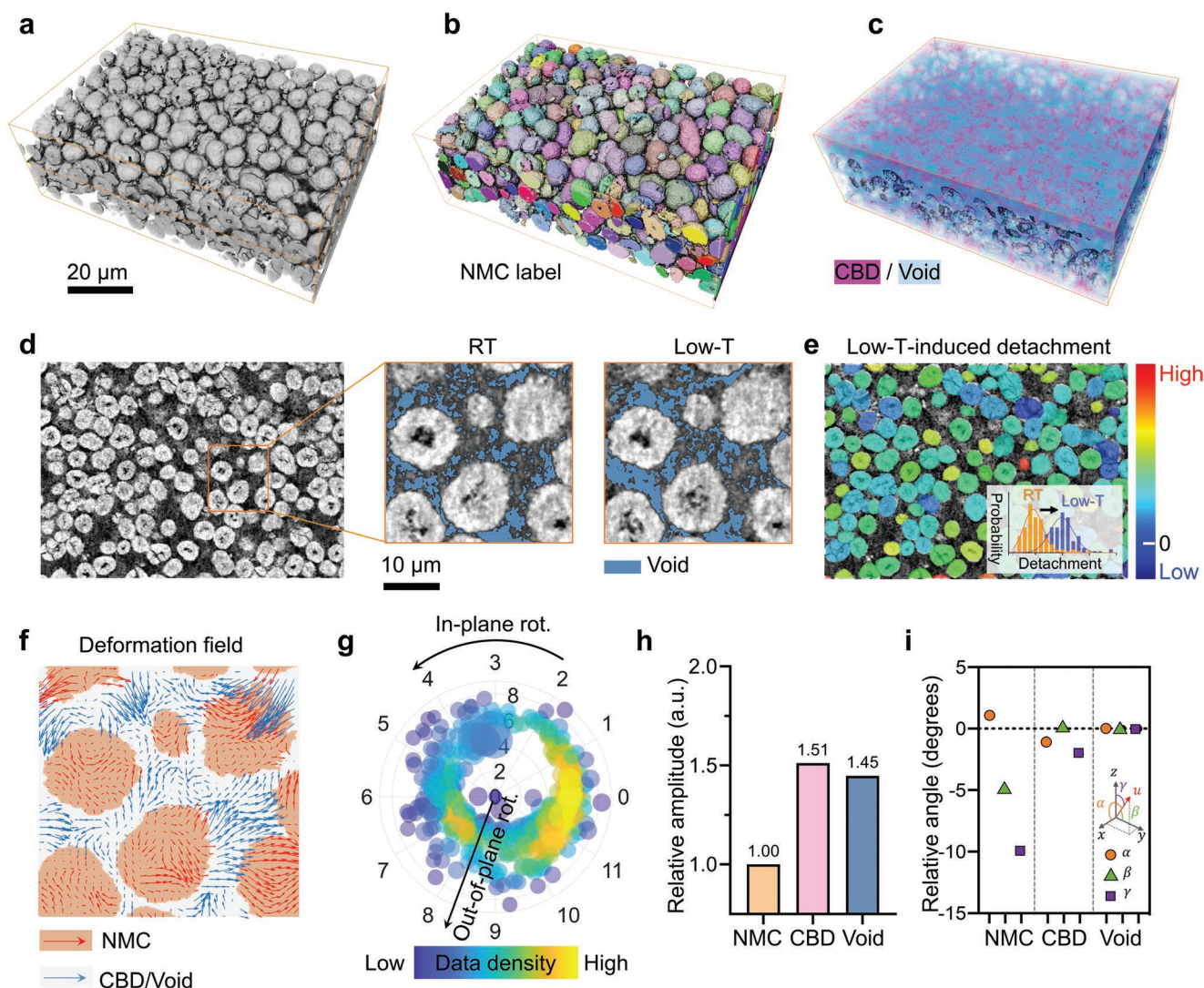


Figure 4. Nano-holo-tomography characterization of the composite cathode. a) 3D visualization of the X-ray phase-contrast nano-holo-tomographic data on the composite cathode with the identified NMC particles and segmented inactive phases, for example, CBD and Void, shown in (b,c), respectively. d) A representative lateral virtual slice with an enlarged region of interest compared before and after the low-temperature exposure. e) The detachment caused by low-temperature exposure is calculated particle by particle and the corresponding value is used to color code the map in panel (e). f) The visualization of the low-temperature-induced structural deformation field over the region of interest shown in panel (d). g) The statistical distribution of the deformation vectors' orientations (in degrees) of all NMC particles. h) The relative amplitudes of different phases of deformation normalized to that of the NMC particles. i) The relative angle of different phases' deformation normalized to that of the void phase.

particle level, the damages brought by electrochemical cycling and by the low-temperature exposure show anticorrelated patterns with different degree of association with the pre-existing porosity. The electrode-scale microstructure characterization further shed some light on the effects of CBD matrix deformation. We observed that the low-temperature environment deforms the NMC, CBD, and the pore structure in a rather incoherent fashion, which leads to the particle detachment from the CBD matrix that could significantly degrade the LIB's fast-charging performance. A schematic illustration of our observations on the damage mechanisms of the battery cathode under low-temperature conditions is shown in **Figure 5**. This work presents a fundamental understanding of the mechanisms behind the irreversible performance degradation of LIBs

upon exposure to extremely low temperature. In addition to the structure damages, from practical perspective, methods also need to be established to ensure the solubility of electrolyte salts at a wide temperature range.

4. Experimental Section

NMC Electrode Synthesis and Electrochemical Testing: Composite NMC electrodes containing $\text{LiNi}_{0.8}\text{Mn}_{0.1}\text{Co}_{0.1}\text{O}_2$ (NMC811) and $\text{LiNi}_{0.4}\text{Mn}_{0.4}\text{Co}_{0.2}\text{O}_2$ (NMC442) (50:50 in weight) were casted on the carbon-coated aluminum foil by making a slurry of 90% active material, 5% acetylene black, and 5% polyvinylidene difluoride (PVDF) in the N-methyl-2-pyrrolidone (NMP) solvent. The electrodes were dried in a vacuum oven overnight at 120 °C. CR2032 coin cells with Li anode and

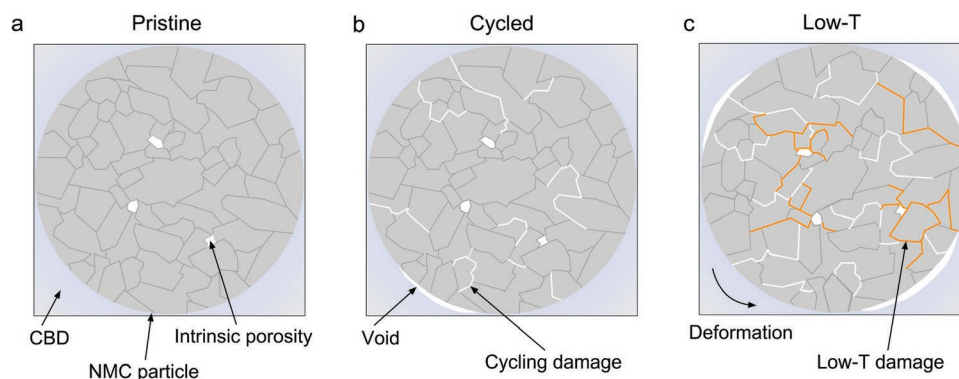


Figure 5. Schematic illustration of the damage mechanisms of the composite battery cathode upon exposure to low-temperature conditions. Prior to the exposure to low-temperature conditions (a-b), the electrochemical cycling induces cracks and some degree of particle detachment from the CBD. The low-temperature exposure further induces particle cracking and CBD deformation (c). In addition, the low-temperature environment deforms the NMC and CBD in an incoherent fashion, exacerbating the particle detachment from the CBD matrix.

NMC cathode were assembled with 1.0 M LiPF₆ dissolved in EC and EMC (3:7 in weight plus 2% VC as additive) as the electrolyte and Whatman glass fiber (1827-047934-AH) as the separator. The coin cells were evaluated on the Wuhan Land battery testing system. All cells were cycled under C/10 (1 C = 200 mAh g⁻¹) for the first cycle as an activation process. After that, they were subjected to 20 cycles under 1 and 5 C, and stored under different temperatures (25, 0, -20, and -80 °C) for two days followed by resting at 25 °C for another two days. Then electrochemical tests were resumed to evaluate the performance after T-storage process.

XAFS and XRD Measurements: XANES and EXAFS are measured at beamline 7-3 at Stanford Synchrotron Radiation Lightsource (SSRL) with a dedicated helium cryostat. Ni foils were used to calibrate all the XAFS data. The EXAFS data were processed using the ATHENA module implemented in the IFEFFIT software package. The ARTEMIS module of IFEFFIT was used to do curve-fitting analysis. The low-temperature XRD measurement was performed at beamline 14-1 of SSRL.

Full-Field TXM Measurement: The nano-tomography of the single secondary particle of the charged NMC811 material was performed using the transmission X-ray microscopy (TXM) at the beamline 6-2c of SSRL. The nominal spatial resolution of TXM is ≈30 nm. The sample holder was rotated from -90° to 90° with an angular step size of 0.5°. More details of the synchrotron beamline configuration can be found elsewhere.^[24] The experimental setup is shown in Figure S12, Supporting Information. The cryo-jet is used to deliver cold air on one side of the sample. We used a Cu pipe (connected to a vacuum cleaner) to suck the cold air away on the other side of the sample. The cryo-jet delivers cold air with dry N₂ shielding to avoid sample icing. The TXM data processing was performed using an in-house developed software package known as TXM-Wizard.^[25] The segmentation and visualization of the 3D data were carried out using a commercial software package known as Avizo.

X-Ray Phase-Contrast Nano-Tomography: The X-ray phase-contrast nano tomography experiments were conducted at the ID16A-NI nano-imaging beamline at the European Synchrotron Radiation Facility (ESRF) in Grenoble, France. This beamline features a high energy hard X-ray nano-probe,^[26] delivering a focus down to ≈20 nm with a brilliant photon flux (up to 10¹² photons s⁻¹ at ΔE/E ≈ 1%). The nano-focus is achieved by two pairs of multilayer-coated Kirkpatrick-Baez (KB) optics, working at 17 and 33.6 keV, respectively. For every tomography scan, 1500 projections were acquired with 0.2 s exposure time. One complete phase contrast nano-tomography scan constitutes tomograms at four different focus-to-sample distances. These tomograms were subsequently used for phase retrieval to generate 2D phase maps.^[19] The 2D phase maps retrieved from all angular projections were then used as input for a tomographic reconstruction based on the filtered back-projection algorithm method (ESRF PyHST software package^[27]).

NMC Particle Segmentation and 3D Deformation Quantification: The NMC particles were identified through the machine-learning approach

presented in Jiang et al.,^[21] where a pretrained neural network model was applied to current data. The deformation estimation was done by the standard 3D Lucas-Kanade method.^[23] The following optical flow constraint equation for the displacement vectors u , v and w is solved by performing a weighted, least-square fit to a constant model for $[u, v, w]^T$ in each small block of the input volumes: $I_x u + I_y v + I_z w = -I_t$, where I_x, I_y, I_z and I_t are the partial derivatives of the tomography electron density data in a $n \times n \times n$ neighborhood centered with respect to position (x, y, z) and time t . A constant velocity $\vec{V} = (V_x, V_y, V_z)$ is assumed in that neighborhood and the following problem will be minimized:

$$\vec{V}^* = \arg \min_{\vec{V}} \sum_{x,y,z \in \Omega} G^2(x,y,z) \left[\nabla I(x,y,z) \cdot \vec{V}^T + I_t(x,y,z,t) \right]^2 \quad (1)$$

where $G(x, y, z)$ represents a Gaussian windowing function. The above problem can be solved efficiently by setting up a system of equations:

$$\vec{V}^* = [A^T G^2 A]^{-1} A^T G B \quad (2)$$

where the diagonal elements of $G \in \mathbb{R}^{N \times N}$ are the predefined 3D Gaussian coefficients, $N = n^3$ represents the number of voxels in the local volume, the N rows of $A \in \mathbb{R}^{N \times 3}$ consist of I_x, I_y and I_z for each (x, y, z) position and the N rows of $B \in \mathbb{R}^{N \times 1}$ consist of the $-I_t$ values for those (x, y, z) positions.

The angles and amplitudes are subsequently extracted from the 3D vectors for each voxel at three different components.

Supporting Information

Supporting Information is available from the Wiley Online Library or from the author.

Acknowledgements

J.L., S.L., and Y.Z. contributed equally to this work. Use of the Stanford Synchrotron Radiation Lightsource, SLAC National Accelerator Laboratory, is supported by the U.S. Department of Energy, Office of Science, Office of Basic Energy Sciences under Contract No. DE-AC02-76SF00515. The hard X-ray phase contrast tomography was conducted at the Nano-Imaging beamline ID16A-NI at the ESRF, Grenoble, France. F.L. acknowledges support from the National Science Foundation under the Grants DMR-1832613 and CBET-1912885. K.Z. is grateful for the support of the National Science Foundation through the grant DMR-1832707.

The engineering support from D. Van Campen, D. Day, and V. Borzenets for the TXM experiment at beamline 6-2C of SSRL is gratefully acknowledged.

Conflict of Interest

The authors declare no conflict of interest.

Data Availability Statement

The data that support the findings of this study are available from the corresponding author upon reasonable request.

Keywords

chemomechanics, lithium-ion batteries, low temperatures, structural deformation, synchrotron characterization

Received: July 13, 2021
Revised: August 2, 2021
Published online:

- [1] A. Gupta, A. Manthiram, *Adv. Energy Mater.* **2020**, *10*, 2001972.
- [2] J. Hou, M. Yang, D. Wang, J. Zhang, *Adv. Energy Mater.* **2020**, *10*, 1904152.
- [3] M.-T. F. Rodrigues, G. Babu, H. Gullapalli, K. Kalaga, F. N. Sayed, K. Kato, J. Joyner, P. M. Ajayan, *Nat. Energy* **2017**, *2*, 17108.
- [4] H. Maleki, J. N. Howard, *J. Power Sources* **2006**, *160*, 1395.
- [5] C.-K. Huang, J. S. Sakamoto, J. Wolfenstine, S. Surampudi, *J. Electrochem. Soc.* **2000**, *147*, 2893.
- [6] S. Wu, R. Xiong, H. Li, V. Nian, S. Ma, *J. Energy Storage* **2020**, *27*, 101059.
- [7] C. T. Love, O. A. Baturina, K. E. Swider-Lyons, *ECS Electrochem. Lett.* **2014**, *4*, A24.
- [8] C. E. L. Foss, A. M. Svensson, Ø. Gullbrekken, S. Sunde, F. Vullum-Bruer, *J. Energy Storage* **2018**, *17*, 395.
- [9] X. Dong, Y. Lin, P. Li, Y. Ma, J. Huang, D. Bin, Y. Wang, Y. Qi, Y. Xia, *Angew. Chem., Int. Ed.* **2019**, *58*, 5623.
- [10] Y. Yang, Y. Yin, D. M. Davies, M. Zhang, M. Mayer, Y. Zhang, E. S. Sablina, S. Wang, J. Z. Lee, O. Borodin, C. S. Rustonji, Y. S. Meng, *Energy Environ. Sci.* **2020**, *13*, 2209.
- [11] J. Xu, X. Wang, N. Yuan, J. Ding, S. Qin, J. M. Razal, X. Wang, S. Ge, Y. Gogotsi, *Energy Storage Mater.* **2019**, *23*, 383.
- [12] X. Dong, Z. Guo, Z. Guo, Y. Wang, Y. Xia, *Joule* **2018**, *2*, 902.
- [13] M. M. Besli, S. Xia, S. Kuppan, Y. Huang, M. Metzger, A. K. Shukla, G. Schneider, S. Hellstrom, J. Christensen, M. M. Doeff, Y. Liu, *Chem. Mater.* **2018**, *31*, 491.
- [14] C. Wei, S. Xia, H. Huang, Y. Mao, P. Pianetta, Y. Liu, *Acc. Chem. Res.* **2018**, *51*, 2484.
- [15] S. Xia, L. Mu, Z. Xu, J. Wang, C. Wei, L. Liu, P. Pianetta, K. Zhao, X. Yu, F. Lin, Y. Liu, *Nano Energy* **2018**, *53*, 753.
- [16] J. Zhang, Q. Wang, S. Li, Z. Jiang, S. Tan, X. Wang, K. Zhang, Q. Yuan, S.-J. Lee, C. J. Titus, K. D. Irwin, D. Nordlund, J.-S. Lee, P. Pianetta, X. Yu, X. Xiao, X.-Q. Yang, E. Hu, Y. Liu, *Nat. Commun.* **2020**, *11*, 6342.
- [17] C. Tian, D. Nordlund, H. L. Xin, Y. Xu, Y. Liu, D. Sokaras, F. Lin, M. M. Doeff, *J. Electrochem. Soc.* **2018**, *165*, A696.
- [18] Y. Mao, X. Wang, S. Xia, K. Zhang, C. Wei, S. Bak, Z. Shadik, X. Liu, Y. Yang, R. Xu, P. Pianetta, S. Ermon, E. Stavitski, K. Zhao, Z. Xu, F. Lin, X. Yang, E. Hu, Y. Liu, *Adv. Funct. Mater.* **2019**, *29*, 1900247.
- [19] P. Cloetens, W. Ludwig, J. Baruchel, D. V. Dyck, J. V. Landuyt, J. P. Guigay, M. Schlenker, *Appl. Phys. Lett.* **1999**, *75*, 2912.
- [20] Y. Yang, R. Xu, K. Zhang, S. Lee, L. Mu, P. Liu, C. K. Waters, S. Spence, Z. Xu, C. Wei, D. J. Kautz, Q. Yuan, Y. Dong, Y. Yu, X. Xiao, H. Lee, P. Pianetta, P. Cloetens, J. Lee, K. Zhao, F. Lin, Y. Liu, *Adv. Energy Mater.* **2019**, *9*, 1900674.
- [21] Z. Jiang, J. Li, Y. Yang, L. Mu, C. Wei, X. Yu, P. Pianetta, K. Zhao, P. Cloetens, F. Lin, Y. Liu, *Nat. Commun.* **2020**, *11*, 2310.
- [22] P. Cloetens, W. Ludwig, E. Boller, L. Helfen, L. Salvo, R. Mache, M. Schlenker, *P Soc Photo-Opt Ins* **2002**, *4503*, 82.
- [23] B. D. Lucas, T. Kanade, presented at *Proc. 7th Intl. Joint Conf on Artificial Intelligence*, Vancouver, Canada, August **1981**, p. 674.
- [24] F. Meirer, J. Cabana, Y. Liu, A. Mehta, J. C. Andrews, P. Pianetta, *J. Synchrotron Radiat.* **2011**, *18*, 773.
- [25] Y. Liu, F. Meirer, P. A. Williams, J. Wang, J. C. Andrews, P. Pianetta, *J. Synchrotron Radiat.* **2012**, *19*, 281.
- [26] J. C. da Silva, A. Pacureanu, Y. Yang, S. Bohic, C. Morawe, R. Barrett, P. Cloetens, *Optica* **2017**, *4*, 492.
- [27] A. Mirone, E. Brun, E. Gouillart, P. Tafforeau, J. Kieffer, *Nucl. Instrum. Methods Phys. Res., Sect. B* **2014**, *324*, 41.